
SELF-SUPERVISED PATH PLANNING IN UNSTRUCTURED ENVIRONMENTS VIA GLOBAL-GUIDED DIFFERENTIABLE HARD CONSTRAINT PROJECTION

Ziqian Wang

Chenxi Fang

Zhen Zhang *

January 28, 2026

ABSTRACT

Deploying deep learning agents for autonomous navigation in unstructured environments faces critical challenges regarding safety, data scarcity, and limited computational resources. Traditional solvers often suffer from high latency, while emerging learning-based approaches struggle to ensure deterministic feasibility. To bridge the gap from embodied to embedded intelligence, we propose a self-supervised framework incorporating a differentiable hard constraint projection layer for runtime assurance. To mitigate data scarcity, we construct a Global-Guided Artificial Potential Field (G-APF), which provides dense supervision signals without manual labeling. To enforce actuator limitations and geometric constraints efficiently, we employ an adaptive neural projection layer, which iteratively rectifies the coarse network output onto the feasible manifold. Extensive benchmarks on a test set of 20,000 scenarios demonstrate an 88.75% success rate, substantiating the enhanced operational safety. Closed-loop experiments in CARLA further validate the physical realizability of the planned paths under dynamic constraints. Furthermore, deployment verification on an NVIDIA Jetson Orin NX confirms an inference latency of 94 ms, showing real-time feasibility on resource-constrained embedded hardware. This framework offers a generalized paradigm for embedding physical laws into neural architectures, providing a viable direction for solving constrained optimization in mechatronics. Source code is available at: <https://github.com/wzq-13/SSHC.git>.

Index Terms—Self-supervised learning, differentiable optimization, runtime assurance, motion planning, embedded intelligence.

1 Introduction

The transition from embodied intelligence to deployable embedded intelligence constitutes a critical frontier in modern mechatronics [1]. In this context, motion planning in unstructured environments stands as a pivotal challenge [2]. Constrained by irregular obstacles and complex vehicle dynamics [3], planners typically struggle to generate trajectories that are both geometrically collision-free and kinematically feasible [4]. Effective operation in such dynamic environments often necessitates probabilistic reasoning [5]. However, bridging the gap between these stochastic models and deterministic mechatronic control loops remains a fundamental barrier. Real-time systems operate under strict temporal deadlines where safe commands must be delivered within the control cycle to maintain closed-loop stability [6, 7]. Consequently, the critical gap lies in developing AI agents that provide runtime assurance by generating feasible, smooth, and safe motions with the timing determinism required for embedded deployment.

Traditional motion planning strategies have established a robust foundation for autonomous navigation. Search-based methods, such as Hybrid A* [8], provide resolution completeness and facilitate global optimality in discretized

* Corresponding author: Z. Zhang (e-mail: zzhang@tsinghua.edu.cn). Ziqian Wang and Zhen Zhang are with the State Key Laboratory of Tribology in Advanced Equipment, Tsinghua University, Beijing 100084, China and are with the Beijing Key Laboratory of Transformative High-end Manufacturing Equipment and Technology, Department of Mechanical Engineering, Tsinghua University, Beijing 100084, China. Chenxi Fang is with the Automotive Electronics Business Unit at Hirain Inc., China.

spaces. Sampling-based algorithms, exemplified by RRT and its variants [9, 10], are highly effective at discovering connectivity within high-dimensional geometries through probabilistic completeness. Optimization-based frameworks [11–13] have set the standard for generating kinematically smooth and dynamically feasible trajectories. Despite these strengths, deploying these iterative solvers on resource-constrained embedded platforms often requires careful trade-offs between algorithmic convergence rates and real-time response, particularly in unstructured environments with non-convex obstacles.

To address these bottlenecks, data-driven methods like Imitation Learning [14, 15] and Deep Reinforcement Learning [16, 17] offer constant-time inference for embedded intelligence. To enhance the security of learning-based methods, recent research has proposed various approaches, generally falling into two categories: soft regularization and post-hoc shielding. The former incorporates collision penalties or risk-aware terms into the loss function or reward structure [18], encouraging the agent to learn safe behaviors implicitly. However, soft constraints lack deterministic guarantees. The latter employs safety filters, such as Control Barrier Functions (CBFs) [19, 20] or predictive safety filters [21, 22], to override unsafe actions during execution. Recent advancements have also integrated Koopman operators to enhance the prediction accuracy of such safety governors under complex dynamics [23]. While effective at preventing imminent collisions, these distinct add-on modules can lead to conservative behaviors or conflicts with the planner’s optimality, potentially inducing deadlocks in cluttered environments.

A distinct stream of research aims to structurally embed rigorous constraints into neural architectures. Broadly, these methods can be categorized into optimization-based approaches that utilize implicit layers or projections [24–26], constrained generative sampling within diffusion models [27, 28], and neuro-symbolic integration that incorporates logical rules [29, 30]. These approaches introduce strong inductive biases, effectively accelerating training convergence and improving the feasibility of generated outputs. For neuro-symbolic methods, abstracting continuous environmental states into discrete symbols for logical reasoning is difficult in complex, unstructured scenarios. Conversely, optimization-based projections are well-suited for continuous control, providing runtime assurance by rectifying outputs onto feasible manifolds. However, without high-level guidance, these local solvers struggle to balance strict safety with goal-directed progress. They often prioritize immediate feasibility, risking stagnation in safe but passive local minima [31].

To bridge this gap, we propose a self-supervised framework that integrates the deterministic constraint handling of differentiable optimization with the global topological guidance of potential fields (shown in Fig. 1). We extend the adaptive neural projection mechanism [25] to handle nonlinear inequality constraints via slack variables, enabling the network to enforce collision avoidance and kinematic boundaries rigorously. Crucially, we couple this with a Global-Guided Artificial Potential Field (G-APF). Serving as a dense supervision signal, the G-APF effectively steers the agent out of local minima, ensuring the projection layer operates on valid initial guesses. This integration ensures that the network not only efficiently generates paths without expert demonstrations but also explicitly enforces the operational safety and feasibility essential for trustworthy embedded mechatronics.

The main contributions of this paper are:

1. We propose a self-supervised framework that eliminates reliance on expert demonstrations. A Global-Guided Artificial Potential Field is introduced to provide dense topological supervision, effectively guiding the agent out of local minima and mitigating the data scarcity issue in unstructured navigation.
2. A differentiable neural projection layer is established to enforce operational safety. It explicitly addresses high-dimensional nonlinear equality and inequality constraints via slack variables and Log-Sum-Exp (LSE) smoothing. It iteratively projects coarse network outputs onto a feasible manifold, acting as a runtime assurance mechanism.
3. The proposed framework is validated via large-scale benchmarks and closed-loop CARLA [32]. The results confirm an 88.75% success rate and a runtime latency of 94 ms on an NVIDIA Jetson Orin NX. This demonstrates a superior trade-off between navigational robustness and computational efficiency compared to representative baselines, validating the potential for real-time mechatronic applications.

2 Problem Formulation

We define the path planning task as generating a sequence of discrete waypoints $\mathcal{P} = \{\mathbf{p}_0, \mathbf{p}_1, \dots, \mathbf{p}_T\}$ in a 2D plane, where $\mathbf{p}_t = [x_t, y_t]^T$. The planner must generate a path connecting the robot’s current state and the target area, while optimizing efficiency, smoothness, and avoiding collisions.

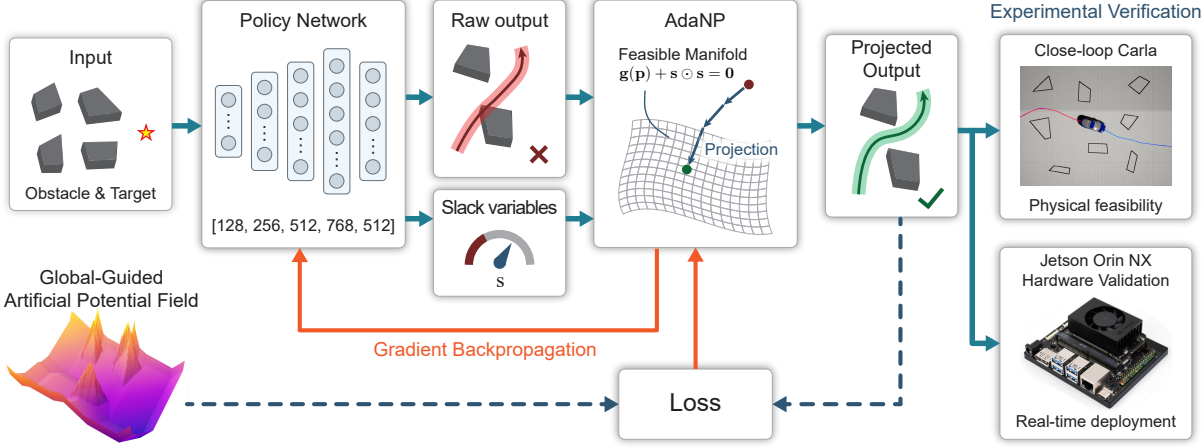


Figure 1: Overall framework of the proposed self-supervised planning system. The architecture integrates a Global-Guided Artificial Potential Field to provide dense supervision signals for the Policy Network during the training phase. To ensure safety, an adaptive-depth neural projection (AdaNP) is embedded in the loop, which rectifies the raw network output into a feasible path by solving the constraint equation $g(\mathbf{p}) + \mathbf{s} \odot \mathbf{s} = \mathbf{0}$.

2.1 Constraints Formulation

2.1.1 Waypoint Density

To guarantee path resolution, the Euclidean distance between consecutive waypoints is constrained by a maximum threshold d_{\max} :

$$\|\mathbf{p}_{t+1} - \mathbf{p}_t\|_2 \leq d_{\max}, \quad \forall t \in \{0, \dots, T-1\}. \quad (1)$$

2.1.2 Kinematic Constraints

The vehicle's steering capability is limited by its physical design. The maximum allowable curvature κ_{\max} is determined by the maximum steering angle δ_{\max} and the wheelbase L :

$$\kappa_{\max} = \tan(\delta_{\max})/L. \quad (2)$$

For the discrete path \mathcal{P} , we calculate the local curvature κ_t at waypoint \mathbf{p}_t using the Menger curvature, which is the inverse of the radius of the circumcircle passing through \mathbf{p}_{t-1} , \mathbf{p}_t , and \mathbf{p}_{t+1} . The constraint requires:

$$|\kappa_t(\mathbf{p}_{t-1}, \mathbf{p}_t, \mathbf{p}_{t+1})| \leq \kappa_{\max}, \quad \forall t \in \{1, \dots, T-1\}. \quad (3)$$

2.1.3 Collision Avoidance

The vehicle must strictly avoid the set of static obstacles \mathcal{O} . For every waypoint \mathbf{p}_t , the distance to the nearest obstacle boundary must exceed the safety radius r_{safe} :

$$\min_{\mathbf{o} \in \mathcal{O}} \|\mathbf{p}_t - \mathbf{o}\|_2 \geq r_{\text{safe}}, \quad \forall t. \quad (4)$$

2.2 Optimization Objective

The planning framework aims to minimize the total travel distance J_{len} and the final deviation from the target J_{goal} , defined as:

$$J_{\text{len}} = \sum_{t=0}^{T-1} \|\mathbf{p}_{t+1} - \mathbf{p}_t\|_2, \quad (5)$$

$$J_{\text{goal}} = \|\mathbf{p}_T - \mathbf{p}_{\text{target}}\|_2^2. \quad (6)$$

3 Methodology

In this section, we present the proposed self-supervised planning framework. As illustrated in Fig. 1, the system comprises three core components: a Global-Guided Potential Field that generates dense supervision signals, a Differentiable Obstacle Representation module that smooths collision constraints, and a Hard Constraint Projection Layer that enforces kinematic and safety feasibility.

3.1 Global-Guided Potential Field

To guide the planned path toward the target while maintaining topological consistency, we construct a dense guidance field $V(\mathbf{u})$ over a grid with 0.2 m resolution (shown in Figure 2). This field serves as a pre-computed supervision signal that provides continuous supervisory signals for the policy network throughout the training process.

First, a global reference path \mathcal{P}^* is generated via Dijkstra's algorithm [33]. We initialize the potential values on \mathcal{P}^* based on their geodesic distance to the goal. Subsequently, we employ a Multi-Source Wavefront Propagation to expand the potential field from \mathcal{P}^* into the free space. The potential value of a node \mathbf{u}_{next} is iteratively updated from its neighbor \mathbf{u}_{curr} :

$$V(\mathbf{u}_{\text{next}}) = \min(V(\mathbf{u}_{\text{next}}), V(\mathbf{u}_{\text{curr}}) + \|\Delta\mathbf{u}\|_2 + V_{\text{obs}}(\mathbf{u}_{\text{next}})), \quad (7)$$

where $\|\Delta\mathbf{u}\|_2$ denotes the Euclidean distance. The term $V_{\text{obs}}(\mathbf{u})$ imposes a high penalty constant within obstacle regions, creating a steep repulsive gradient that drives the optimization toward the safe valley centered on \mathcal{P}^* . This mechanism drastically elevates the potential values within obstacle areas, creating a steep repulsive gradient at the boundaries that effectively pushes the optimization process away from collisions and toward the safe free space.

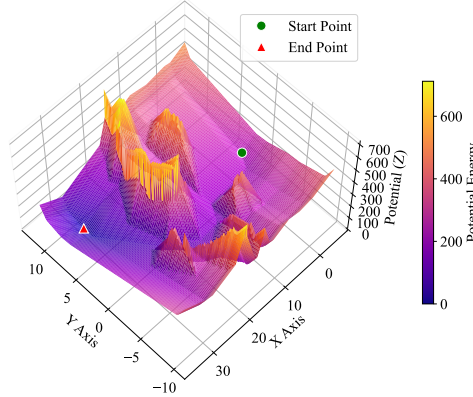


Figure 2: Visualization of the Global-Guided Potential Field. The multi-source wavefront propagation creates a convex valley along the optimal path, providing dense gradient guidance to steer the agent out of local minima.

To drive the agent toward the goal while avoiding local minima, the potential field loss \mathcal{L}_{pot} combines a global gradient term with a local attraction term:

$$\mathcal{L}_{\text{pot}} = \frac{1}{T} \sum_{t=1}^T \left(V_{\text{interp}}(\mathbf{p}_t) + \beta \min_{\mathbf{u} \in \mathcal{N}(\mathbf{n}_t)} \|\mathbf{p}_t - \mathbf{u}\|_2^2 \right). \quad (8)$$

The first term aligns the path with the global energy valley via bilinear interpolation. The second term ($\beta > 0$) pulls the agent toward the local minimum node \mathbf{u} within $\mathcal{N}(\mathbf{n}_t)$, preventing stagnation or oscillations in obstacle-dense regions where the first term's gradient may become nearly orthogonal to the desired direction of progress (shown in Figure 3).

3.2 Differentiable Hard Constraint Projection

We embed hard physical constraints into the network architecture by parameterizing slack variables within the output layer, enabling an end-to-end differentiable projection for constrained optimization.

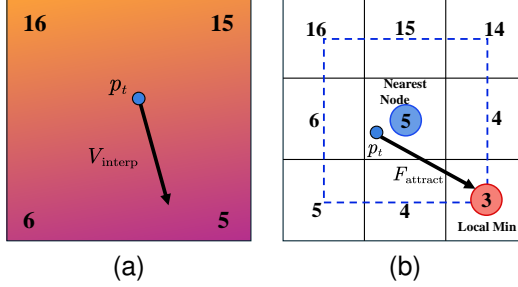


Figure 3: Global-Guided Potential Field Loss. (a) Direct potential minimization guides the agent toward lower potential regions. (b) Local attraction ensures continuous progress along the potential valley, especially in obstacle-dense areas.

3.2.1 Differentiable Collision Representation

To facilitate gradient-based optimization within the projection layer, we approximate the non-differentiable collision boundaries using the LSE technique [34]. Unlike discrete Boolean checks, LSE transforms the collision condition into a smooth, differentiable manifold.

For the j -th obstacle defined by the intersection of M_j half-planes $l_{j,m}(\mathbf{p}) \geq 0$, the signed distance is approximated by $c_j(\mathbf{p}) \approx -\frac{1}{\alpha} \log(\sum_{m=1}^{M_j} e^{-\alpha l_{j,m}(\mathbf{p})})$. The global collision constraint aggregates all N_{obs} obstacles via the smooth maximum operator:

$$C_{\text{obs}}(\mathbf{p}) = \text{LSE}_{\max}(\{c_j(\mathbf{p})\}_j) = \frac{1}{\alpha} \log \left(\sum_{j=1}^{N_{\text{obs}}} e^{\alpha c_j(\mathbf{p})} \right), \quad (9)$$

The feasibility requires $C_{\text{obs}}(\mathbf{p}) < 0$. Here, α is a positive scaling factor controlling the approximation accuracy. Theoretically, as $\alpha \rightarrow \infty$, the LSE function converges to the exact max/min operator. However, excessively large values of α induce sharp transitions in the constraint landscape, resulting in exploding gradients that can destabilize the optimization process. We empirically selected $\alpha = 10$ to strike a balance between geometric fidelity and numerical stability. Visualization is in Supplementary Material.

3.2.2 Differentiable Constraint Transformation

To enable gradient-based projection, we reformulate the inequality constraints defined in Section 2 into equality constraints $\mathbf{h}(\mathbf{y}) = \mathbf{0}$ by introducing augmented slack variables \mathbf{s} . The state vector at time t is expanded to $\mathbf{y}_t = [\mathbf{p}_t^T, \mathbf{s}_t^T]^T$. By enforcing $\mathbf{g}(\mathbf{p}) + \mathbf{s} \odot \mathbf{s} = \mathbf{0}$, the inequality $\mathbf{g}(\mathbf{p}) \leq \mathbf{0}$ is strictly satisfied while maintaining differentiability.

We aggregate the constraints into a unified vector $\mathbf{h}(\mathbf{y}_t)$. For collision avoidance, the vehicle footprint is approximated by three covering circles with centers $\mathbf{c}_{t,k}$, ($k \in \{1, 2, 3\}$) to ensure differentiability. Kinematic and density constraints use squared terms for numerical smoothness:

$$\mathbf{h}(\mathbf{y}_t) = \begin{bmatrix} \text{LSE}_{\max}(\{C_{\text{obs}}(\mathbf{c}_{t,k}) + r_{\text{safe}}\}_{k=1}^3) + s_{t,\text{obs}}^2 \\ \kappa_t^2 - \kappa_{\max}^2 + s_{t,\kappa}^2 \\ \|\mathbf{p}_{t+1} - \mathbf{p}_t\|_2^2 - d_{\max}^2 + s_{t,d}^2 \end{bmatrix} = \mathbf{0}. \quad (10)$$

By concatenating these terms over the horizon T , we define the unified constraint problem $\mathbf{h}(\mathbf{y}) = \mathbf{0}$, which serves as the optimization target for the subsequent projection layer.

3.2.3 Differentiable Projection Layer

We employ a differentiable projection layer based on the Newton-Raphson method to project the coarse network output \mathbf{y}_k onto the feasible manifold defined by $\mathbf{h}(\mathbf{y}) = \mathbf{0}$. This is formulated as a Quadratic Programming (QP) problem:

$$\begin{aligned} \mathbf{y}_{k+1} = & \underset{\mathbf{y}}{\operatorname{argmin}} \quad \frac{1}{2} \|\mathbf{y} - \mathbf{y}_k\|_2^2 \\ \text{s.t.} \quad & \mathbf{h}(\mathbf{y}_k) + \mathbf{J}_{\mathbf{h}}(\mathbf{y}_k)(\mathbf{y} - \mathbf{y}_k) = \mathbf{0}, \end{aligned} \quad (11)$$

where \mathbf{J}_h is the Jacobian matrix. Solving the Lagrangian dual yields the closed-form minimum-norm Newton step:

$$\mathbf{y}_{k+1} = \mathbf{y}_k - \mathbf{J}_h^\dagger(\mathbf{y}_k)\mathbf{h}(\mathbf{y}_k), \quad (12)$$

with the pseudo-inverse $\mathbf{J}_h^\dagger = \mathbf{J}_h^T(\mathbf{J}_h\mathbf{J}_h^T)^{-1}$. This update is applied iteratively until $\|\mathbf{h}(\mathbf{y}_k)\|_\infty < \epsilon$, or the number of steps reaches the maximum iteration limit (I_{\max}). Enforcing a strict iteration cap guarantees deterministic worst-case execution time. Since all operations are differentiable, gradients from \mathbf{y}^* flow to the policy, enabling end-to-end training. To ensure real-time feasibility on embedded GPUs, we optimize the projection solver via static computation graphs and kernel fusion.

3.3 Curriculum Training Strategy

Solving a highly non-convex optimization problem with strict hard constraints from scratch typically leads to severe solver oscillation and gradient instability. To mitigate this, we design a two-stage curriculum learning strategy [35] that progressively increases the difficulty of the constraints.

3.3.1 Stage 1: Soft-Constraint Training

In this stage, the hard projection layer is deactivated. The network learns the global topology and rough path feasibility using soft loss.

The constraints defined in the previous section are relaxed into penalty terms using the ReLU function:

$$\mathcal{L}_{\text{soft_obs}} = \frac{1}{T} \sum_{t,k} \text{ReLU}(C_{\text{obs}}(\mathbf{c}_{t,k}) + r_{\text{safe}}), \quad (13)$$

$$\mathcal{L}_{\text{soft_curve}} = \frac{1}{T} \sum_t \text{ReLU}(|\kappa_t| - \kappa_{\max}), \quad (14)$$

$$\mathcal{L}_{\text{soft_dist}} = \frac{1}{T} \sum_t \text{ReLU}(\|\mathbf{p}_{t+1} - \mathbf{p}_t\|_2 - d_{\max}). \quad (15)$$

To facilitate the transition to the hard-constraint projection in Stage 2, the network must learn to predict appropriate slack variables \mathbf{s} that satisfy the constraints. We introduce an auxiliary loss $\mathcal{L}_{\text{slack}}$:

$$\mathcal{L}_{\text{slack}} = \frac{1}{T} \sum_{t=1}^T |\mathbf{h}(\text{sg}(\mathbf{p}_t), s_{t,\text{obs}}, s_{t,\kappa}, s_{t,d})|, \quad (16)$$

where $\text{sg}(\cdot)$ denotes the stop-gradient operator. Minimizing $\mathcal{L}_{\text{slack}}$ effectively calibrates the slack variables to the environment's topology. This mitigates excessive corrections during projection, thereby reducing the risk of solver oscillation or convergence to suboptimal local minima.

Let $\mathcal{L}_{\text{soft}}$ denote the aggregated soft constraint penalty:

$$\mathcal{L}_{\text{soft}} = \mathcal{L}_{\text{soft_obs}} + \mathcal{L}_{\text{soft_curve}} + \mathcal{L}_{\text{soft_dist}}. \quad (17)$$

The total loss for Stage 1 is then formulated as:

$$\mathcal{L}_{\text{Stage1}} = \mathcal{L}_{\text{pot}} + \mathcal{L}_{\text{slack}} + \lambda_{\text{soft}} \mathcal{L}_{\text{soft}}. \quad (18)$$

3.3.2 Stage 2: Hard-Constraint Projection

Once the network converges to a preliminary solution, we activate the differentiable projection layer. This layer projects the coarse prediction onto the feasible manifold defined by $\mathbf{h}(\mathbf{y}) = \mathbf{0}$.

In this stage, the explicit soft constraint losses and the slack estimation loss are removed. We introduce a projection loss $\mathcal{L}_{\text{proj}}$ to minimize the correction magnitude. The objective becomes:

$$\mathcal{L}_{\text{Stage2}} = \mathcal{L}_{\text{pot}} + \lambda_{\text{proj}} \underbrace{\frac{1}{T} \sum_{t=0}^T \|\hat{\mathbf{y}}_t - \mathbf{y}_t\|_2^2}_{\mathcal{L}_{\text{proj}}}. \quad (19)$$

where $\hat{\mathbf{y}}_t$ is the raw network output and \mathbf{y}_t is the projected feasible output. Minimizing $\mathcal{L}_{\text{proj}}$ aligns the raw output $\hat{\mathbf{y}}_t$ with the feasible projection \mathbf{y}_t . This regularization anchors predictions within the solver's convergence basin, effectively treating the projection as a lightweight local refinement and significantly reducing inference latency. The evolution of the path through these stages is visualized in Fig. 4. The complete training procedure is outlined in Algorithm 1.

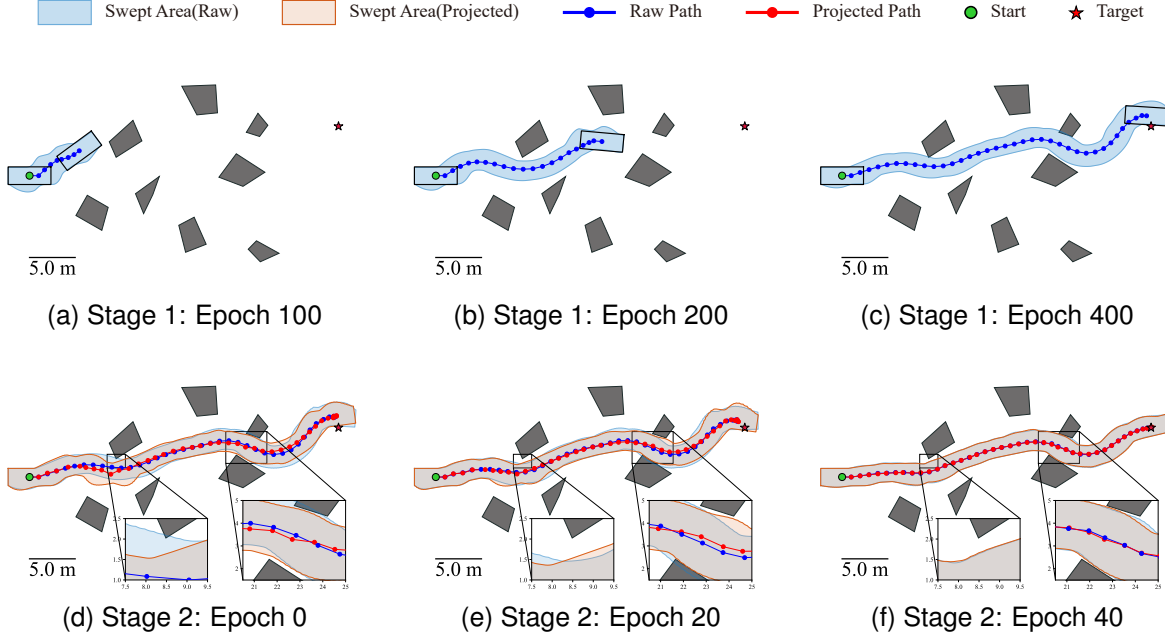


Figure 4: The evolution of the planned path during training. (a)-(c) Stage 1: The network learns to follow the potential valley with soft constraints roughly. (d)-(f) Stage 2: The hard projection layer refines the path to enhance safety and kinematic feasibility.

4 EXPERIMENTS

4.1 Experimental Setup

4.1.1 Environment and Data

We designed challenging experimental scenarios to validate navigation in obstacle-dense unstructured terrains. The ego vehicle is modeled as a kinematic bicycle with a wheelbase $L = 2.8$ m, width $w = 1.9$ m, and maximum steering angle $\delta_{\max} = 0.70$ rad [36]. The environment spans a 40×20 m area, where $N_{\text{obs}} = 8$ random quadrilateral obstacles are generated with side lengths $l \sim \mathcal{U}(1, 4)$ m and goals are randomly sampled within the target area on the right. Details are provided in Supplementary Material. A total of 200,000 scenarios were generated and partitioned into training, validation, and testing sets (6:3:1).

4.1.2 Baselines and Metrics

We compare our framework against four representative baselines. The implementation details and hyperparameters of each baseline are provided in Supplementary Material.

1. Search-based: Hybrid A* [8] utilizing Reeds-Shepp curves for kinematic feasibility.
2. Sampling-based: Informed RRT* [10] with obstacle inflation (1.2 m).
3. Optimization-based: NMPC [37] implemented via the CasADi framework [38] and the IPOPT solver [39], sharing the exact kinematic model and differentiable obstacle representation as our method.
4. Learning-based: IL trained on Hybrid A* expert demonstrations, and a Soft-Constraint network trained without the projection layer. This baseline shares the same network structure and parameters as our method but excludes the slack variables from the output layer.

Performance is evaluated using static metrics: Success Rate (SR; collision-free arrival within 1.0 m), Average Path Length (APL), Computation Time (CT), and Kinematic Compliance ($\mathcal{S}_{\text{kin}} = \sum_{t=1}^T \min(\kappa_{\max}/\kappa_t, 1)/T$).

To validate physical feasibility, we conduct closed-loop tracking experiments in CARLA [32]. The planned paths are tracked by a PID controller. Detailed configurations are provided in Supplementary Material. We report Tracking Success Rate (TSR), Cross-Track Error (RMSE CTE), and Steering Smoothness ($\mathcal{J}_{\text{smooth}} = \sum_{t=0}^{T-1} |\delta_{t+1} - \delta_t|/T$).

Algorithm 1 Two-Stage Self-Supervised Training Strategy

Require: Dataset \mathcal{D} , Pre-computed Potential Field $V(\mathbf{u})$, Weights $\lambda_{\text{soft}}, \lambda_{\text{proj}}$, Epochs E_{S1}, E_{S2} .
Ensure: Safety-Critical Policy Network π_θ .

```

Initialize  $\pi_\theta$  randomly.
for epoch  $e = 1$  to  $E_{S1}$  do
  for batch  $B \in \mathcal{D}$  do
     $\hat{\mathbf{y}} = [\mathbf{x}, \mathbf{s}] \leftarrow \pi_\theta(B)$ .
    Compute  $\mathcal{L}_{\text{total}} = \mathcal{L}_{\text{pot}} + \lambda_{\text{soft}} \mathcal{L}_{\text{soft}} + \mathcal{L}_{\text{slack}}$ .
    Update  $\theta$  via  $\nabla_\theta \mathcal{L}_{\text{total}}$ .
  end for
end for
for epoch  $e = 1$  to  $E_{S2}$  do
  for batch  $B \in \mathcal{D}$  do
     $\hat{\mathbf{y}} \leftarrow \pi_\theta(B)$ 
     $\mathbf{y}_0 \leftarrow \hat{\mathbf{y}}$  {Init projection}
    while  $\|\mathbf{h}(\mathbf{y}_k)\|_\infty > \epsilon$  and  $k < I_{\text{max}}$  do
       $\mathbf{y}_{k+1} \leftarrow \mathbf{y}_k - \mathbf{J}_h^\dagger(\mathbf{y}_k) \mathbf{h}(\mathbf{y}_k)$ 
       $k \leftarrow k + 1$ .
    end while
    Update  $\theta$  via  $\nabla_\theta (\mathcal{L}_{\text{pot}} + \lambda_{\text{proj}} \|\hat{\mathbf{y}}_0 - \mathbf{y}_k\|_2^2)$ .
  end for
end for
return  $\pi_\theta$ 

```

Table 1: Comparative Analysis of Path Planning Performance

Category	Method	CT (s) [†]	APL (m)	SR (%)	\mathcal{S}_{kin}	AFD (m)
Rule-based	Hybrid A*	12.3392	35.57	98.80	0.9999	0.00
	Informed RRT*	9.4949	34.59	86.26	0.9650	0.00
Optimization	NMPC	1.5308	34.47	82.35	0.9969	0.00
Learning-based	IL (Pure)	0.0014	33.52	12.40	0.9921	0.57
	IL + Soft	0.0014	33.45	54.30	0.9998	1.25
	Soft	0.0014	33.31	55.22	0.9976	0.88
	Hard (Ours)	0.0939	33.30	88.75	0.9885	0.53

[†] CT for Learning-based methods is measured on Jetson Orin NX, while other baselines are measured on the Intel i9-14900KF CPU.

Bold values indicate the best results for each metric.

4.1.3 Implementation Details

The policy network is a five-layer MLP with hidden dimensions [128, 256, 512, 768, 512] and ReLU activations trained using Adam [40]. Training consists of a soft-constraint pre-training stage (400 epochs, $lr = 10^{-4}$, batch size 256) followed by a hard-constraint refinement stage (40 epochs, $lr = 10^{-5}$, batch size 64). During inference, the hard projection layer uses a tolerance of $\epsilon = 10^{-3}$ with a maximum 50 iterations. Training utilized an Intel i9-14900KF CPU and NVIDIA RTX 2080 Ti GPU. For inference, learning-based methods were deployed on an NVIDIA Jetson Orin NX, while traditional planners were evaluated on the Intel i9-14900KF CPU.

4.2 Comparative Analysis of Planning Performance

Table 1 presents a quantitative evaluation across 20,000 scenarios. The results reveal that existing methods face distinct limitations. Search-based Hybrid A* excels in completeness, achieving a 98.80% success rate. However, this comes at the cost of prohibitive latency (> 12 s), caused by the exponential expansion of motion primitives in the search space. Conversely, pure learning methods provide negligible computation times (≈ 1.4 ms) but struggle with safety. Lacking explicit geometric constraints, their success rate drops below 55%. As for optimization-based NMPC, while it incorporates constraints, it achieves only an 82.35% success rate. This performance cap arises because the solver frequently gets trapped in local minima due to its high sensitivity to initialization.

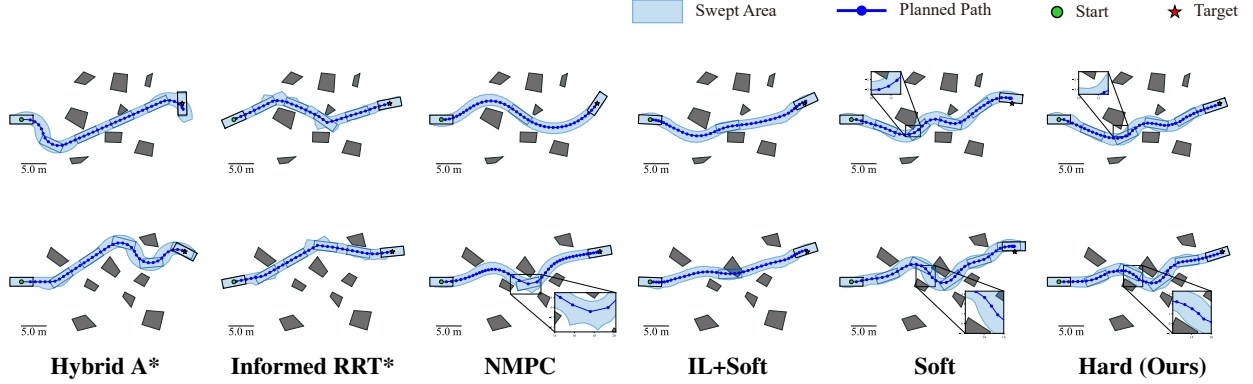


Figure 5: Qualitative comparison of generated paths in two narrow-corridor scenarios (top and bottom rows). As highlighted in the zoomed-in regions: the NMPC baseline exhibits sparse waypoint distribution, which poses a risk of collision during actual execution due to interpolation errors. The comparison between the Soft and Hard methods demonstrates the effectiveness of the proposed hard constraint formulation in strictly guaranteeing collision-free swept areas within tight spaces.

Table 2: Comparative Analysis of Path Tracking Performance

Method	RMSE CTE (m)	Max CTE (m)	AHE (°)	DFR (%)	$\mathcal{J}_{\text{smooth}}$	TSR (%)	SR Drop (%)
Hybrid A*	0.2505	0.6102	5.122	96.25	0.0335	94.65	4.15
Informed RRT*	0.2715	0.6090	6.619	94.70	0.0311	62.55	23.71
NMPC	0.1041	0.2441	4.367	98.53	0.0312	74.48	7.87
IL+Soft	0.1473	0.3214	4.184	99.56	0.0429	44.35	9.95
Soft	0.1860	0.4149	6.276	98.02	0.0371	41.70	12.45
Hard (Ours)	0.1982	0.4544	5.823	97.70	0.0377	80.40	8.35

Bold values indicate the best results for each metric.

Our framework strikes a superior balance between computational efficiency and safety guarantees. By integrating a differentiable projection layer designed to explicitly enforce hard constraints, our method achieves an 88.75% success rate, significantly outperforming NMPC. Unlike Informed RRT*, which generates stochastic and often jagged paths, our method produces deterministic and smoother paths, as evidenced by the superior Average Path Length (33.30 m). Computationally, our method maintains an efficient inference latency of 0.0939 s on the Jetson Orin NX, achieving an acceleration of over two orders of magnitude compared to Hybrid A* running on Intel i9-14900KF. This efficiency explicitly validates the method’s suitability for resource-constrained embedded systems.

4.3 Dynamic Validation and Path Tracking

Table 2 summarizes the dynamic validation results obtained from 2,000 testing scenarios.

4.3.1 Tracking Robustness and Feasibility Gap

As shown in Table 2, Hybrid A* establishes the benchmark with a Tracking Success Rate (TSR) of 94.65%. In contrast, pure learning baselines (IL+Soft and Soft) fail to ensure safety (< 45% TSR), and NMPC (74.48%) frequently stagnates in local minima. Our framework achieves a TSR of 80.40%. A key metric here is the *SR Drop*, which quantifies the degradation from static planning to dynamic execution. Informed RRT* suffers a drastic drop of 23.71%, indicating that its geometrically feasible paths are often dynamically infeasible. Conversely, our method maintains a minimal SR Drop of 8.35%. By integrating kinematic constraints into the projection process, our method guarantees dynamically feasible paths that result in superior tracking performance.

4.3.2 Control Accuracy and Stability

In terms of tracking precision, NMPC achieves the lowest RMSE CTE (0.1041 m) due to its explicit model-based formulation. While Soft baselines yield low tracking errors, this is primarily because they generate overly smooth paths that violate obstacle constraints, resulting in high failure rates despite precise tracking.

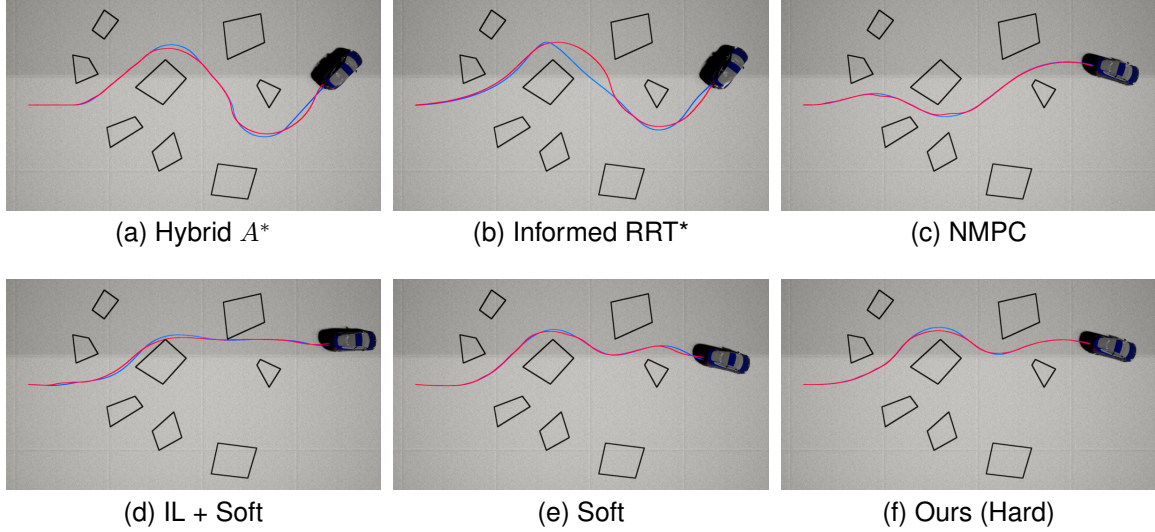


Figure 6: Visual comparison of path tracking in CARLA. Obstacles are depicted as black polygons, while blue and red lines denote planned paths and actual tracking trajectories, respectively. Note that Hybrid A^* (a) exhibits control oscillations during continuous turns, and Informed RRT* (b) suffers from large tracking errors due to infeasible sharp turns. The Soft baselines (d, e) fail to avoid obstacles effectively. In contrast, both NMPC (c) and our method (f) demonstrate high kinematic feasibility while strictly ensuring operational safety.

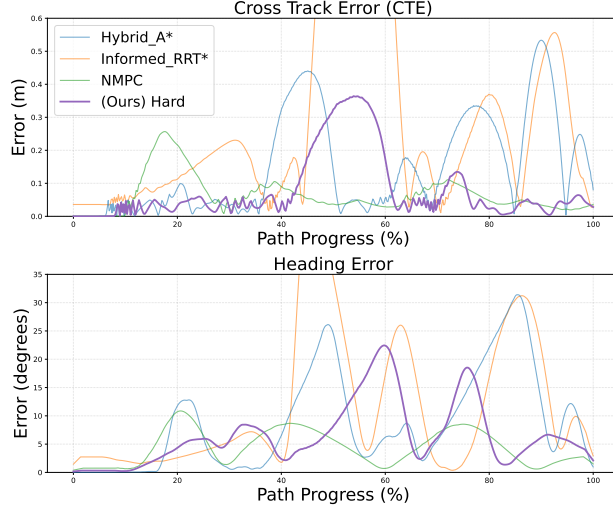


Figure 7: Tracking error analysis. Our method (black line) maintains low cross-track and heading errors throughout the trajectory, mitigating the oscillations seen in Hybrid A^* and the spikes in RRT*.

Our method maintains a competitive RMSE CTE of 0.1982 m. Notably, this accuracy surpasses both Hybrid A^* (0.2505 m) and Informed RRT* (0.2715 m). As visualized in Fig. 6(a), Hybrid A^* relies on Reeds-Shepp primitives, which introduce curvature discontinuities at junction points. Our method exhibits a high Dynamic Feasibility Ratio (DFR: 97.7%) and superior smoothness. This confirms the high physical feasibility of the paths generated by our method.

4.4 Ablation Studies and Sensitivity Analysis

To comprehensively evaluate the robustness of the proposed framework and verify the contribution of its core modules, we investigated the impact of three critical factors: λ_{soft} in the pre-training stage, I_{\max} of the hard constraint projection layer, and the fundamental necessity of the G-APF.

Table 3: Ablation Study of Soft Constraint Weighting (λ_{soft})

λ_{soft}	CT (s)	APL (m)	SR (%)	\mathcal{S}_{kin}	AFD (m)
0.5	0.0014	33.18	48.82	0.9975	1.0250
0.8	0.0014	33.34	50.04	0.9971	1.0560
1.0	0.0014	33.36	52.22	0.9974	1.0224
1.2	0.0014	33.31	55.22	0.9976	0.8785
1.5	0.0014	13.61	0.00	0.7825	18.9200

4.4.1 Impact of λ_{soft}

The weight λ_{soft} balances obstacle avoidance and goal attraction during pre-training. As shown in Table 3, increasing λ_{soft} from 0.5 to 1.2 steadily improves SR, indicating that stronger penalties effectively encourage obstacle-aware representations. However, a threshold exists; at $\lambda_{\text{soft}} = 1.5$, the planner becomes overly conservative, trapping the agent in local minima (0% SR) due to excessive repulsive forces. Consequently, we selected $\lambda_{\text{soft}} = 1.2$ as the optimal balance between safety awareness and goal reachability.

Table 4: Ablation Study of Projection Iterations (I_{max})

I_{max}	CT (s)	APL (m)	SR (%)	\mathcal{S}_{kin}	AFD (m)
20	0.0427	33.36	87.01	0.9872	0.5081
50	0.0939	33.32	88.75	0.9885	0.5345
80	0.1245	33.30	89.58	0.9889	0.5465
100	0.1363	33.30	89.84	0.9890	0.5719

4.4.2 Impact of I_{max}

Table 4 examines the trade-off between solvability and computation time. Increasing I_{max} from 20 to 50 significantly boosts SR (87.01% to 88.75%) and reduces AFD. However, further increasing iterations to 100 yields diminishing returns ($\approx 1\%$ SR gain) at the cost of increased computational overhead. To satisfy the real-time constraint of autonomous navigation in unstructured environments, we fixed $I_{\text{max}} = 50$ as the optimal compromise between kinematic feasibility and efficiency.

Table 5: Ablation Study on Global-Guided Potential Field

Method	CT (s)	APL (m)	SR	\mathcal{S}_{kin}	AFD (m)
w/o G-APF	0.0010	12.98	0.00%	0.9918	21.95
Hard (Ours)	0.2079	33.30	88.75%	0.9885	0.53

4.4.3 Impact of G-APF

To verify the necessity of the proposed global guidance, we replaced the G-APF with a standard Euclidean distance heuristic. Table 5 reveals that the Euclidean baseline yields a 0.00% SR. This zero success rate is attributed to the agent getting trapped in local minima and consequently failing to reach the goal, rather than collisions, as evidenced by the large AFD of 21.95 m. Note that the second-stage projection was omitted for this baseline because the hard constraint layer cannot converge without a coarse-feasible initial guess.

5 CONCLUSION

This paper proposes a self-supervised path planning framework designed for embedded mechatronics in unstructured environments. By coupling global topological guidance with differentiable constraint projection, the proposed architecture achieves data-efficient learning and explicit runtime safety without requiring expert demonstrations. Extensive experiments and embedded deployment on an NVIDIA Jetson Orin NX validate the system’s performance, achieving an 88.75% success rate with a real-time latency of 94 ms.

Future work will extend this embedded intelligence framework to dynamic environments by integrating motion prediction into Spatio-Temporal Potential Fields, enabling safe interaction with moving agents. Additionally, we plan to investigate hybrid search-learning strategies to provide robust warm starts for the projection solver, further enhancing the system's resilience and convergence reliability in extreme mechatronic operating conditions.

Acknowledgments

This work was supported in part by National Natural Science Foundation of China under Grant 52275564, U24A20109, and by Beijing Natural Science Foundation under Grant QY24251.

The authors would like to thank Chengyun Ju, Donggang Sang, and Bingtao Zhang from Hirain Inc. for their valuable discussions and technical support during the course of this work.

References

- [1] Yang Liu, Weixing Chen, Yongjie Bai, Xiaodan Liang, Guanbin Li, Wen Gao, and Liang Lin. Aligning cyber space with physical world: A comprehensive survey on embodied ai. *IEEE-ASME Trans. Mechatron.*, 2025.
- [2] Yuqing Guo, Zelin Guo, Yazhou Wang, Danya Yao, Bai Li, and Li Li. A survey of trajectory planning methods for autonomous driving—part i: Unstructured scenarios. *IEEE Trans. Intell. Veh.*, 9(9):5407–5434, 2024.
- [3] Xuanzuo Liu, Anil K Madhusudhanan, and David Cebon. Minimum swept-path control for autonomous reversing of a tractor semi-trailer. *IEEE Trans. Veh. Technol.*, 68(5):4367–4376, 2019.
- [4] Giorgia Chiriatti, Giacomo Palmieri, Cecilia Scoccia, Matteo Claudio Palpacelli, and Massimo Callegari. Adaptive obstacle avoidance for a class of collaborative robots. *Machines*, 9(6):113, 2021.
- [5] Ching-Wei Chuang and Harry H Cheng. A novel approach with bayesian networks to multi-robot task allocation in dynamic environments. In *Proc. ASME Int. Des. Eng. Tech. Conf. Comput. Inf. Eng. Conf.*, volume 85444, page V08AT08A047. American Society of Mechanical Engineers, 2021.
- [6] Yu Zhang, Linghuan Kong, Xinbo Yu, Wei He, and Alois Knoll. Robust dual-filter safety control for mobile robots in dynamic multiobstacle environments. *IEEE-ASME Trans. Mechatron.*, 2025.
- [7] Kaikai Zheng, Dawei Shi, and Yang Shi. Safety-critical randomized event-triggered learning of gaussian process with applications to data-driven predictive control. *IEEE Trans. Autom. Control.*, 70(6):3920–3935, 2025.
- [8] Dmitri Dolgov, Sebastian Thrun, Michael Montemerlo, and James Diebel. Path planning for autonomous vehicles in unknown semi-structured environments. *Int. J. Robot. Res.*, 29(5):485–501, 2010.
- [9] Sertac Karaman and Emilio Frazzoli. Sampling-based algorithms for optimal motion planning. *Int. J. Robot. Res.*, 30(7):846–894, 2011.
- [10] Jonathan D. Gammell, Siddhartha S. Srinivasa, and Timothy D. Barfoot. Informed RRT*: Optimal sampling-based path planning focused via direct sampling of an admissible ellipsoidal heuristic. In *Proc. IEEE/RSJ Int. Conf. Intell. Robots Syst.*, pages 2997–3004, Chicago, IL, USA, 2014.
- [11] Bai Li, Yakun Ouyang, Li Li, and Youmin Zhang. Autonomous driving on curvy roads without reliance on Frenet frame: A Cartesian-based trajectory planning method. *IEEE Trans. Intell. Transp. Syst.*, 23(9):15729–15741, 2022.
- [12] Zijun Guo, Yuanxin Wang, Huilong Yu, and Junqiang Xi. Fast optimization-based trajectory planning with cumulative key constraints for automated parking in unstructured environments. *IEEE Trans. Veh. Technol.*, 74(8):11820–11831, 2025.
- [13] Xiangyu Zhang, Yi Wang, Bingxian Mu, and Se Young Yoon. Empc-based flight control and collision-free path planning for a quadrotor with unbalanced payload. *IEEE-ASME Trans. Mechatron.*, 30(6):5745–5754, 2025.
- [14] Yinan Zheng, Ruiming Liang, Kexin Zheng, Jinliang Zheng, Liyuan Mao, Jianxiong Li, Weihao Gu, Rui Ai, Shengbo Eben Li, Xianyuan Zhan, and Jingjing Liu. Diffusion-based planning for autonomous driving with flexible guidance. In *Proc. Int. Conf. Learn. Represent.*, Singapore, 2025.
- [15] Zhigen Zhao, Shuo Cheng, Yan Ding, Ziyi Zhou, Shiqi Zhang, Danfei Xu, and Ye Zhao. A survey of optimization-based task and motion planning: From classical to learning approaches. *IEEE-ASME Trans. Mechatron.*, 2024.
- [16] Gang Chen, Yue Zhang, Liangmo Wang, and Weigong Zhang. Gaussian mixture model and deep reinforcement learning based driving robot system gearshift strategy with vehicle longitudinal driving states. *IEEE-ASME Trans. Mechatron.*, 29(6):4549–4559, 2024.

- [17] Yechen Zhang, Bin Gao, Gang Wang, Jian Sun, and Zhuo Li. Corb-planner: Corridor as observations for rl planning in high-speed flight. *IEEE-ASME Trans. Mechatron.*, 30(6):4070–4080, 2025.
- [18] Xiangkun He, Jingda Wu, Zhiyu Huang, Zhongxu Hu, Jun Wang, Alberto Sangiovanni-Vincentelli, and Chen Lv. Fear-neuro-inspired reinforcement learning for safe autonomous driving. *IEEE Trans. Pattern Anal. Mach. Intell.*, 46(1):267–279, 2024.
- [19] Mingyu Cai and Cristian-Ioan Vasile. Safety-critical learning of robot control with temporal logic specifications. *IEEE Trans. Autom. Control*, 70(8):5553–5560, 2025.
- [20] Changzhu Zhang, Lifei Dai, Hao Zhang, and Zhuping Wang. Control barrier function-guided deep reinforcement learning for decision-making of autonomous vehicle at on-ramp merging. *IEEE Trans. Intell. Transp. Syst.*, 26(6):8919–8932, 2025.
- [21] Yifan Zhou, Yixuan Zhou, Kefan Jin, and Hesheng Wang. Hierarchical reinforcement learning with model guidance for mobile manipulation. *IEEE-ASME Trans. Mechatron.*, 30(6):6155–6163, 2025.
- [22] Federico Pizarro Bejarano, Lukas Brunke, and Angela P. Schoellig. Safety filtering while training: Improving the performance and sample efficiency of reinforcement learning agents. *IEEE Robot. Autom. Lett.*, 10(1):788–795, 2025.
- [23] Hao Chen, Xiangkun He, Shuo Cheng, and Chen Lv. Deep koopman operator-informed safety command governor for autonomous vehicles. *IEEE-ASME Trans. Mechatron.*, 29(5):3568–3578, 2024.
- [24] Priya Donti, David Rolnick, and J. Zico Kolter. DC3: A learning method for optimization with hard constraints. In *Proc. Int. Conf. Learn. Represent.*, 2021.
- [25] Giacomo Lastrucci and Artur M. Schweidtmann. ENFORCE: Nonlinear constrained learning with adaptive-depth neural projection. *arXiv preprint arXiv:2502.06774*, 2025.
- [26] Ashfaq Iftakher, Rahul Golder, Bimol Nath Roy, and M.M. Faruque Hasan. Physics-informed neural networks with hard nonlinear equality and inequality constraints. *Comput. Chem. Eng.*, 204:109418, 2026.
- [27] Vince Kurtz and Joel W. Burdick. Equality constrained diffusion for direct trajectory optimization. In *Proc. Amer. Control Conf.*, pages 535–540, Denver, CO, USA, 2025.
- [28] Nic Fishman, Leo Klarner, Emile Mathieu, Michael Hutchinson, and Valentin De Bortoli. Metropolis sampling for constrained diffusion models. In *Adv. Neural Inf. Process. Syst.*, volume 36, pages 62296–62331, 2023.
- [29] Eleonora Giunchiglia, Alex Tatomir, Mihaela Cătălina Stoian, and Thomas Lukasiewicz. Ccn+: A neuro-symbolic framework for deep learning with requirements. *Int. J. Approx. Reason.*, 171:109124, 2024. Synergies between Machine Learning and Reasoning.
- [30] Wenguan Wang, Yi Yang, and Fei Wu. Towards data-and knowledge-driven ai: A survey on neuro-symbolic computing. *IEEE Trans. Pattern Anal. Mach. Intell.*, 47(2):878–899, 2025.
- [31] Long Jin, Shuai Li, Bin Hu, and Mei Liu. A survey on projection neural networks and their applications. *Appl. Soft Comput.*, 76:533–544, 2019.
- [32] Alexey Dosovitskiy, German Ros, Felipe Codevilla, Antonio Lopez, and Vladlen Koltun. CARLA: An open urban driving simulator. In *Proc. Conf. Robot Learn.*, pages 1–16, Mountain View, CA, USA, 2017.
- [33] Edsger W. Dijkstra. A note on two problems in connexion with graphs. *Numer. Math.*, 1(1):269–271, 1959.
- [34] Stephen P. Boyd and Lieven Vandenberghe. *Convex Optimization*. Cambridge Univ. Press, Cambridge, U.K., 2004.
- [35] Yoshua Bengio, Jérôme Louradour, Ronan Collobert, and Jason Weston. Curriculum learning. In *Proc. Int. Conf. Mach. Learn.*, pages 41–48, Montreal, QC, Canada, 2009.
- [36] Philip Polack, Florent Altché, Brigitte d’Andréa Novel, and Arnaud de La Fortelle. The kinematic bicycle model: A consistent model for planning feasible trajectories for autonomous vehicles? In *Proc. IEEE Intell. Veh. Symp.*, pages 812–818, Los Angeles, CA, USA, 2017.
- [37] James Blake Rawlings, David Q. Mayne, Moritz Diehl, et al. *Model Predictive Control: Theory, Computation, and Design*, volume 2. Nob Hill Publishing, Madison, WI, USA, 2020.
- [38] Joel A. E. Andersson, Joris Gillis, Greg Horn, James B. Rawlings, and Moritz Diehl. CasADi: A software framework for nonlinear optimization and optimal control. *Math. Program. Comput.*, 11(1):1–36, 2019.
- [39] Andreas Wächter and Lorenz T. Biegler. On the implementation of an interior-point filter line-search algorithm for large-scale nonlinear programming. *Math. Program.*, 106(1):25–57, 2006.
- [40] Diederik P. Kingma and Jimmy Ba. Adam: A method for stochastic optimization. In *Proc. Int. Conf. Learn. Represent.*, San Diego, CA, USA, 2015.